Extreme Mechanics Letters 77 (2025) 102356

Contents lists available at ScienceDirect

Extreme Mechanics Letters

journal homepage: www.elsevier.com/locate/eml

Hexagonal tessellation-based mechanical metamaterials

Reza Moghimimonfared, Andrea Spaggiari, Luigi Grasselli, Luke Mizzi *

Department of Sciences and Methods for Engineering, University of Modena and Reggio Emilia, Reggio Emilia, Italy

ARTICLE INFO

Keywords:
Auxetic metamaterials
Hexagonal tessellations
Honeycomb structures
Additive manufacturing

ABSTRACT

Mechanical metamaterials based on Euclidean polygonal tessellations represent a new class of architectured materials with the potential to exhibit a wide range of mechanical properties. In this work, we investigate a new class of systems based on the generic hexagonal tessellation with trigonal rotational symmetry and show how this tessellation has the potential to exhibit a wide range of Poisson's ratios, including auxeticity, as well as a large spectrum of Young's moduli whilst retaining transverse isotropy. The tessellation was characterized through geometric expressions in order to identify which combination of geometric parameters lead to realizable, concave or convex configurations and Finite Element simulations were used to evaluate the mechanical properties of these tessellations. Furthermore, three additively-manufactured prototypes, representative of the entire Poisson's ratio range (i.e. negative, zero and positive Poisson's ratio) were experimentally tested and analysed using Digital Image Correlation. The results obtained from both simulation and experimental approaches demonstrate the mechanical capabilities of these tessellations and indicate how new auxetic metamaterials may be found by exploring the vast design space afforded by Euclidean polygonal tilings.

1. Introduction

Mechanical metamaterials are a class of man-made structured materials which have the ability to exhibit counterintuitive behaviors that are rarely found in nature. These peculiar behaviors arise from their structure rather than material composition [1,2]. Research on mechanical metamaterials is typically focused on systems with unusual (negative or zero) values of four mechanical properties [3]. These include the three elastic constants: Young's modulus (E), shear modulus (G) and bulk modulus (K); and a dimensionless parameter, the Poisson's ratio (ν). Metamaterials which fall under the latter class are called auxetic metamaterials. They are architected materials possessing a negative Poisson's ratio, which means that contrary to conventional positive Poisson's ratio materials, they have the potential to expand in the lateral direction when stretched uniaxially and contract globally when compressed [4–6]. This property enhances the indentation resistance and energy absorption characteristics of these materials, while also inducing synclastic out-of-plane deformation behavior. These useful secondary characteristics have opened up numerous possibilities for implementation of auxetic metamaterials in specialized applications such as endovascular stents and other biomedical implants, as well as personal protection and sports equipment requiring lightweight structures with a large energy absorption potential for protection from impact [7–10], to name a few.

Auxetic metamaterials can be broadly classified under four major categories. These include re-entrant configurations [11–15], chiral honeycombs [16–30], rotating rigid units [31–40], and origami structures [41,42]. These classes comprise structures with various symmetries and forms which are periodically tessellated in 2D or 3D space. Many of these tessellations are based on hexagonal configurations. For example, re-entrant hexagonal honeycombs are formed from concave hexagonal cells with two arrow-shaped or inward-facing angles. The Poisson's ratio of these systems can be controlled as a function of the re-entrancy angle, with systems having a positive internal angle (i.e. convex honeycombs) possessing a positive Poisson's ratio (Fig. 1a) and systems having a negative internal angle (i.e. concave honeycombs) exhibiting auxetic behavior [43,44] (Fig. 1b). Hexagonal cell geometries are also found in rotating unit and chiral systems. In the former class, the rotating triangle system [45] in its fully-opened state is a case in point (see Fig. 1e), while for chiral honeycombs, trichiral and anti-trichiral [19] systems are both based on hexagonal tessellations (see Fig. 1c and d). The mechanical properties of these systems can also be varied considerably by changing the geometric parameters of the structures and they possess the potential to exhibit a wide spectrum of Poisson's ratios ranging from positive to large negative values. Besides these systems, other hierarchical metamaterials and systems based on

* Corresponding author.
E-mail address: luke.mizzi@unimore.it (L. Mizzi).

https://doi.org/10.1016/j.eml.2025.102356
Received 21 March 2025; Received in revised form 2 May 2025; Accepted 16 May 2025
Available online 21 May 2025

multi-polygonal tessellations with hexagonal cells which show auxetic behavior [26,46,47] have also been designed [34] (see Fig. 1f).

Although numerous studies have been conducted on the mechanical properties of hexagon-based structures such as the ones shown in Fig. 1, there are many other forms which have yet to be explored. From a purely geometric point of view, three general types of monohedral hexagonal tessellations may be formed in 2D space (shown in Fig. 2), hereby denoted as Type I, Type II and Type III [48,49]. These forms, each of which have different symmetry characteristics, afford a large design space which is still relatively unknown in terms of metamaterial design and potential to exhibit auxetic behaviour.

In view of this, in this work we aim to address this lacuna in the state-of-the-art by conducting a parametric investigation on these hexagonal systems. Specifically, we focus on the Type III tessellation which is characterized by an in-plane trigonal rotational symmetry and an absence of an axis of mirror-symmetry, a combination which is not commonly found in auxetic metamaterial tessellations. This tessellation was chosen since its symmetry characteristic is expected to impart transverse isotropy on the system, unlike Type I and Type II tessellations which are expected to be considerably anisotropic. The main goal was to analyse the mechanical properties and deformation behaviour of this tessellation type by investigating the influence of geometric parameters on these characteristics and identify possible configurations which yield auxetic properties. This was done through a comprehensive Finite Element (FE) simulation run on various hexagonal structures followed by experimental verifications on additively-manufactured prototypes.

2. Methodology

In this section, we first describe the design approach used to construct these hexagonal tessellations with trigonal rotational symmetry. In this regard, we demonstrate the geometrical rules that govern the formation of the tessellation as well as the geometric limitations that define its realizability and the conditions required to create either a concave or convex hexagonal shape. Next, we discuss how we used FE to simulate and examine the mechanical properties of the various hexagonal tessellations we designed. Finally, the experimental procedure used to validate the results obtained from the finite element simulations is described. By following this structured methodology, we aim to comprehensively explore and discuss the mechanical properties of the proposed irregular hexagonal tiling.

2.1. Design of trigonal symmetry hexagonal tessellations

As stated previously, there are three general forms of monohedral hexagonal tessellations; shown in Fig. 2. The Type I and Type II systems are characterized by a rotational symmetry of order 2 and consist of two and four different orientations of hexagons periodically replicated in space, respectively. The Type III tessellation, which is the object of this study, on the other hand, possesses trigonal rotational symmetry, as depicted in Fig. 2.

A schematic representation of the hexagonal tessellation investigated in this study is shown in Fig. 3. In order to build this tessellation, a monohedral tessellation defined by three independent variables, i, j, and k, is utilized. In addition, a number of specific geometric requirements must be satisfied. As shown in Fig. 3, the hexagon consists of a consecutive pair of sides with length i (AB and BC), a consecutive pair with length j (EF and FA), and a consecutive pair with length k (CD and DE). The interior angle between these pairs of sides must be 120°, while the remaining interior angles may vary (i.e., the angles between the sides with lengths i and j, j and k, and k and i). In addition to this condition, the chosen combination of i, j and k values must result in a realizable triangle ACE. This means that not every combination of i, j, and k will result in a tessellable hexagon. These two general conditions may be summarized in Eqs. (1) and (2).

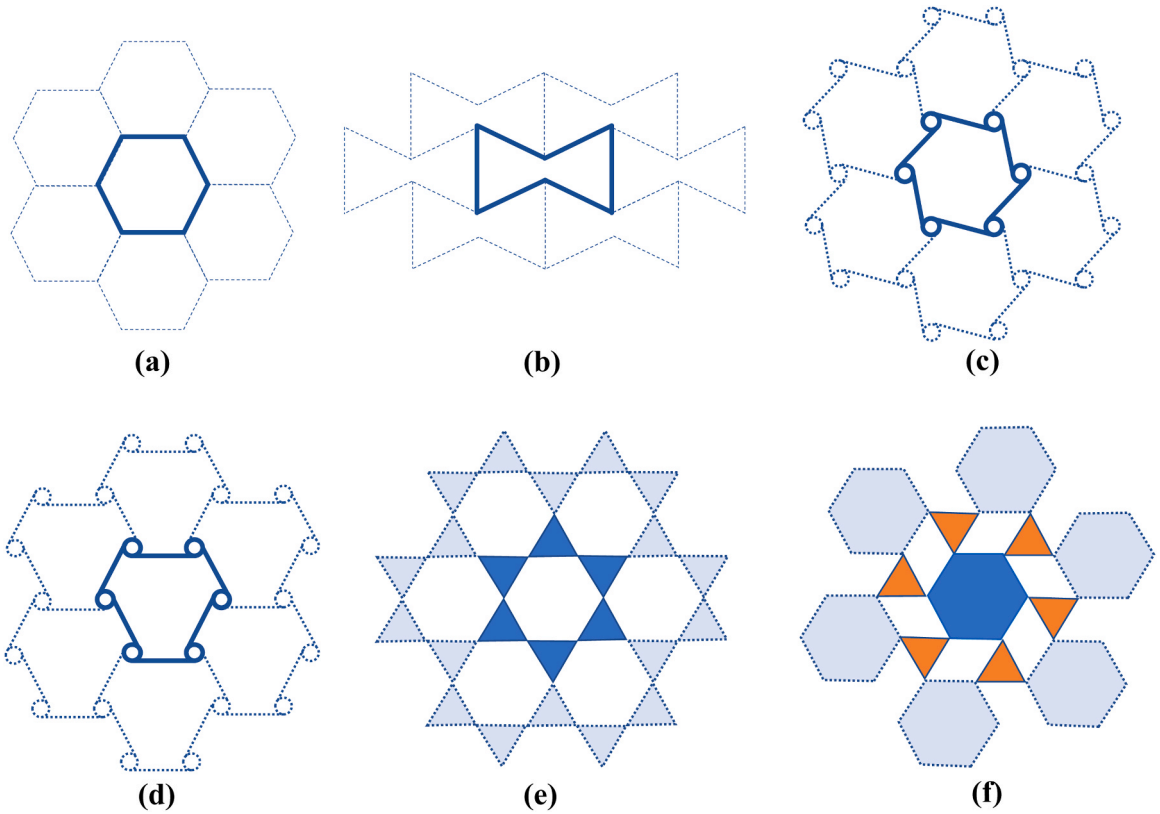

Fig. 1. Utilizing hexagonal configurations to design different types of metamaterials; (a) Regular hexagonal, (b) Re-entrant, (c) Trichiral, (d) Anti-trichiral, (e) Triangle rotating unit, and (f) Hexagon triangle rotating units.

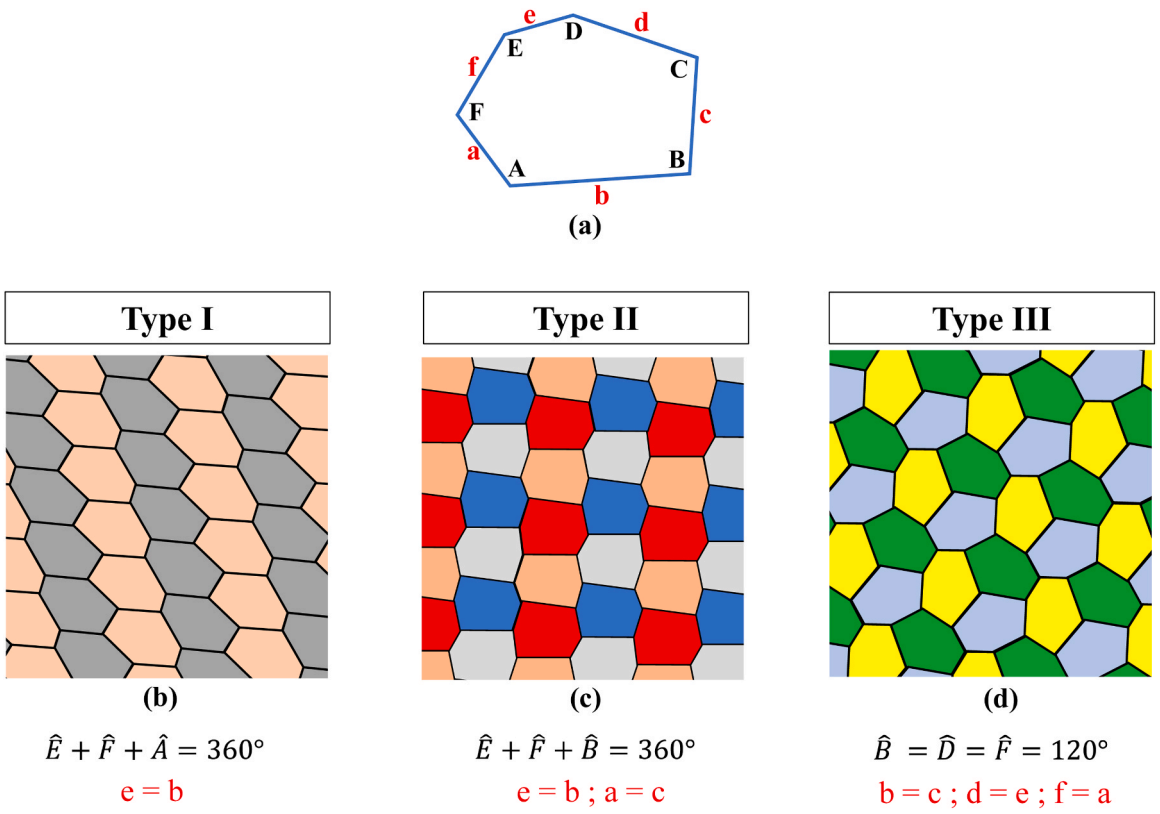

Fig. 2. Three general forms of hexagonal tessellations: (a) Generic hexagon, (b) Type I, (c) Type II, (d) Type III (adapted from [48]).

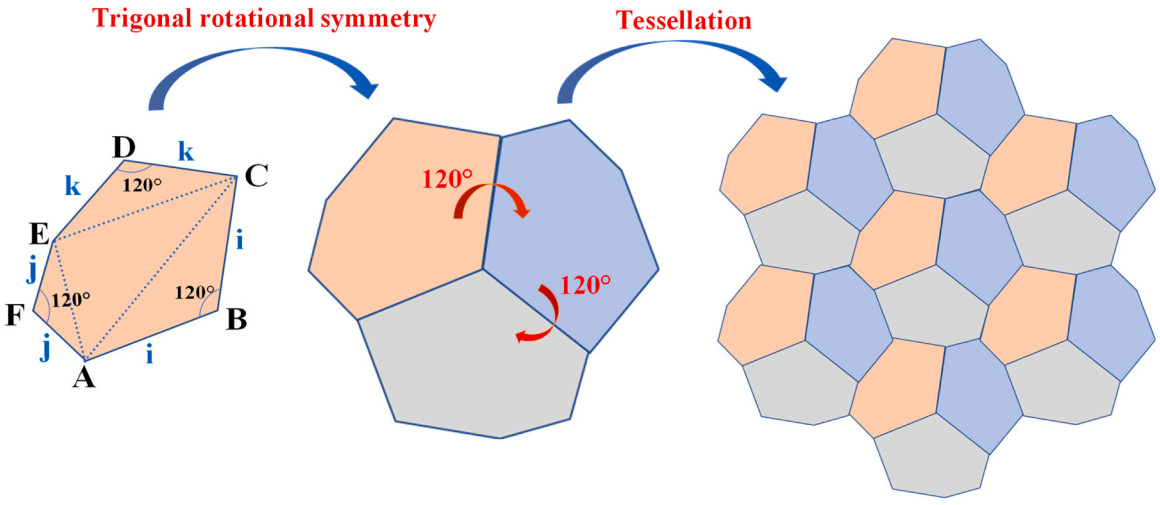

Fig. 3. A trigonal rotational symmetry and tessellation of a single hexagonal tessellation of Type III.

a) Geometry of the hexagon must consist of three pairs of consecutive equal sides, and the angle between these sides of equal length is 120°; therefore,

$$\begin{aligned} AB = BC = i, \quad & \measuredangle ABC = 120^\circ \\ EF = FA = j, \quad & \measuredangle EFA = 120^\circ \\ CD = DE = k, \quad & \measuredangle CDE = 120^\circ \end{aligned} \tag{1}$$

b) Realizability condition: Connecting the vertices created by the intersection of two unequal sides (vertices C, E, and A) of the hexagon yields four (or in special cases, three) internal triangles, comprising three lateral isosceles triangles (ABC, CDE, and EFA) and one central triangle (ACE). The central triangle's side lengths are AC= $\sqrt{3}$i, EA = $\sqrt{3}$j, and CE = $\sqrt{3}$k. Considering the central part as either a triangle or a line, the selected combination of side lengths i, j, and k must meet the following realizability condition:

$$\begin{cases} i+j \geq k \\ i+k \geq j \\ j+k \geq i \end{cases} \Rightarrow \quad |i-j| \leq k \leq i+j \qquad (i,j,k>0) \tag{2}$$

In mathematical literature, typically another rule is added: the three lateral isosceles triangles ABC, CDE and EFA must be formed externally to the triangle ACE. This rule holds for all the cases shown in Fig. 4,

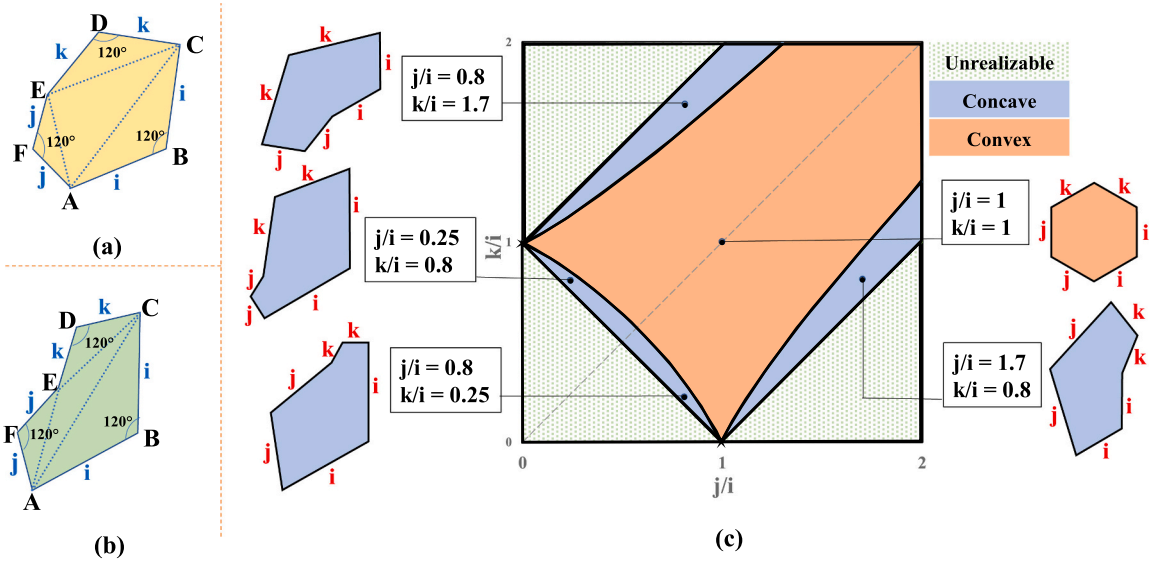

Fig. 4. A schematic representation of the labeled hexagon considered in this study features trigonal rotational symmetry besides the realizable area for various combinations of i, j, and k: (a) convex, (b) concave, and (c) realizable area.

however, as detailed later on, in some cases it may be relaxed, i.e. isosceles triangles may be formed internally to the triangle ACE, and still form a realizable hexagonal tessellation.

As one can observe in Fig. 4c, the design space afforded by these conditions allows for both convex and concave hexagonal tilings, with convex configurations being the most common type. Convex hexagons are characterized by internal angles less than 180°, and all the diagonals of such a hexagon are internally contained. Concave hexagons, which have at least one interior angle greater than 180°, are less common but still allowed. In order to understand which combination of *i*, *j*, and *k* yields convex and concave configurations, the three unknown interior angles of the hexagon ($\measuredangle BCD, \measuredangle DEF$ and $\measuredangle FAB$) can be calculated through the general cosine rule according to Eq. (3)–(5). These equations are plotted in Fig. 4c, where the limits related to convex and concave shapes are clearly evident.

1) Convexity based on the vertex C; $\measuredangle BCD > 180°$

$$\measuredangle BCD = \measuredangle ACE + \frac{\pi}{3} = \arccos\left(\underbrace{\frac{i^2+j^2-k^2}{2ij}}_{\theta}\right) + \frac{\pi}{3}^{\theta>\frac{2\pi}{3}} - 1$$
$$\leq \underbrace{\frac{i^2+j^2-k^2}{2ij} < -\frac{1}{2}}_{\text{ConvexityCondition}}$$

ConvexityCondition :

$$\frac{i^2+j^2-k^2}{2ij} < -\frac{1}{2} \rightarrow \left(\frac{k}{i}\right)^2 > \left(\frac{j}{i}\right)^2 + \left(\frac{j}{i}\right) + 1 \tag{3}$$

2) Convexity based on the vertex E; $\measuredangle DEF > 180°$

$$\measuredangle DEF = \measuredangle CEA + \frac{\pi}{3} = \arccos\left(\underbrace{\frac{i^2+k^2-j^2}{2ik}}_{\theta}\right) + \frac{\pi}{3}^{\theta>\frac{2\pi}{3}} - 1$$
$$\leq \underbrace{\frac{i^2+k^2-j^2}{2ik} < -\frac{1}{2}}_{\textit{Convexity}\text{Condition}}$$

ConvexityCondition :

$$\frac{i^2+k^2-j^2}{2ik} < -\frac{1}{2} \rightarrow \left(\frac{k}{i}\right) < \sqrt{\left(\frac{j}{i}\right)^2 - \left(\frac{3}{4}\right)} - \frac{1}{2} \tag{4}$$

3) Convexity based on the vertex A; $\measuredangle FAB > 180°$

$$\measuredangle FAB = \measuredangle EAC + \frac{\pi}{3} = \arccos\left(\underbrace{\frac{j^2+k^2-i^2}{2jk}}_{\theta}\right) + \frac{\pi}{3}^{\theta>\frac{2\pi}{3}} - 1$$
$$\leq \underbrace{\frac{j^2+k^2-i^2}{2jk} < -\frac{1}{2}}_{\textit{Convexity}\text{Condition}}$$

*Convexity*Condition :

$$\frac{j^2+k^2-i^2}{2jk} < -\frac{1}{2} \rightarrow \left(\frac{k}{i}\right) < \frac{1}{2}\left(\sqrt{4-3\left(\frac{j}{i}\right)^2} - \frac{j}{i}\right) \tag{5}$$

Some examples of different concave and convex hexagons and the resultant tessellations are depicted in Fig. 5. In this figure, the first row shows the single hexagons, while in the second and third rows, schematics of their trigonal rotational symmetry and tessellations, including representative unit cells (RUCs), are indicated, respectively.

A generic convex configuration is shown in Fig. 5a. This is the most common form of structure and its design space is represented by the central orange section in Fig. 4c. In addition to this, a number of concave configurations are also possible, shown by the blue region in Fig. 4c. The external boundary lines of this plot denote the cases where the triangle ACE degenerates into a straight line. These configurations are obtained when the equality conditions of the inequalities in Eq. (2) are met, i.e., $i = j + k$, $j = i + k$, and $k = i + j$.

In the example illustrated in Fig. 5c, angle AEC is equal to 180°.

As mentioned previously, some hexagonal tessellations may be formed by placing the isosceles triangles internal to the central triangle. These cases are particularly rare and represent a very small part of the design space. An example of one such system is shown in Fig. 5d. This tessellation, which has the same *i*, *j* and *k* values as the tessellation shown in Fig. 5b, is formed by placing all three isosceles triangles internally to the central triangle AEC. This means that for a very select

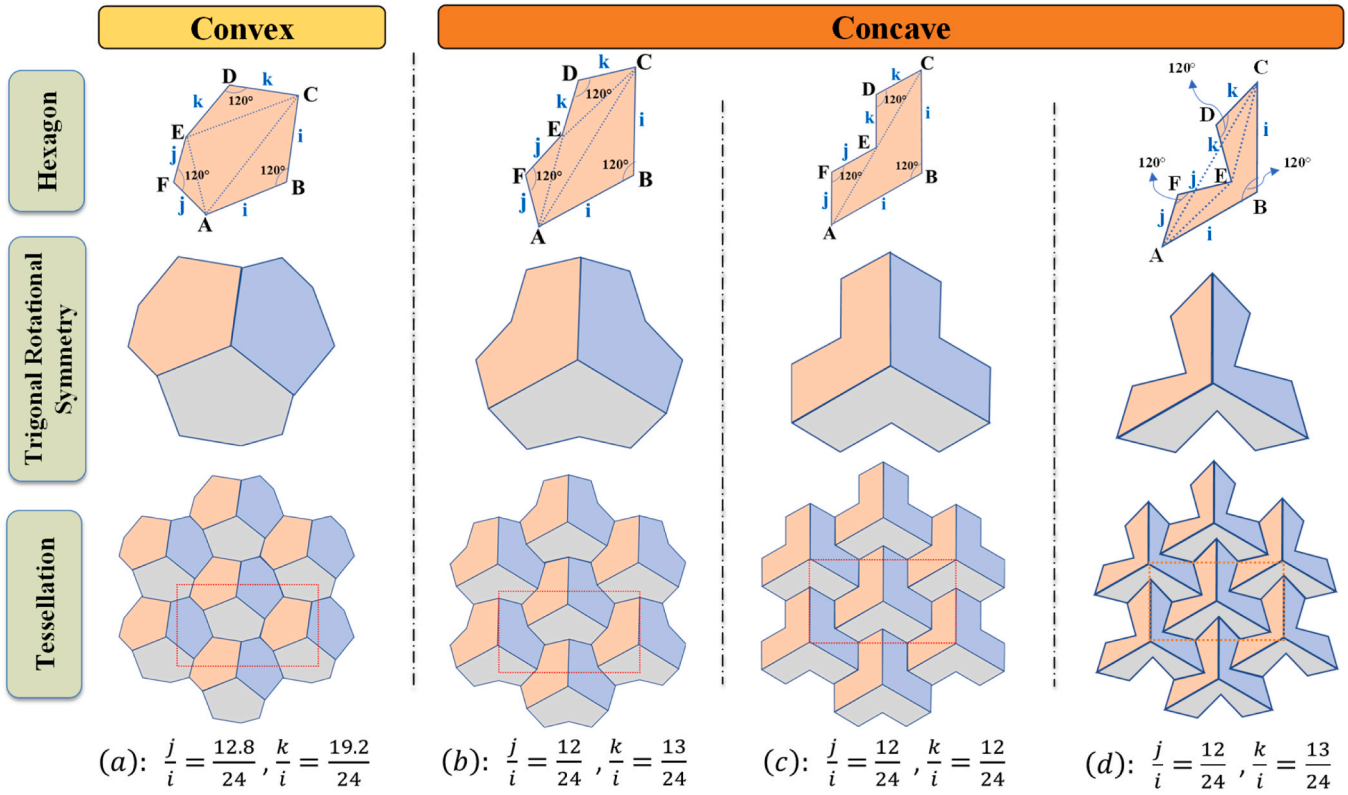

Fig. 5. Some examples of different concave and convex hexagons and the resultant tessellations.

number of configurations with specific i, j and k values, two different tessellations may be obtained. This occurs only in blue regions shown in Fig. 4c, i.e. the concave configurations, since for the convex systems, internal triangles cannot be formed without violating the conditions defined in Eq. (1). Given that these particular forms are not very common; in this work we will focus primarily on the concave structures formed by creating the isosceles triangles external to the central triangle and, unless stated otherwise, any reference to a concave tessellation with a specific i, j and k value pertains to this case.

2.2. Parametric investigation using finite element simulation

In order to investigate the mechanical properties of these tessellations, finite element method (FEM) simulations were carried out on a wider range of configurations. In order to produce a sufficiently large amount of structures necessary for a parametric simulation run to cover the allowed design space, various combinations of i, j, and k were used. Given that the influence of geometric parameters on mechanical properties is mainly related to the ratios of the independent variables, i was set to a constant value of 24 mm while j and k were varied from the range of 1.2–84 mm (corresponding to 0.05(i) to 3.5(i)) in steps of 0.05 (i). Since not all combinations of variables are expected to result in realizable geometries due to mathematical constraints defined in Eq. (2)., the actual number of simulated systems is less than that allowed by the factorial design space. In addition, to these geometric variables, the ligament was defined by a constant rectangular cross-section with an in-plane thickness, t, of 0.1 mm and an out-of-plane depth, d, of 1 mm. A comprehensive list of all stated parameters with their values is presented in Table 1.

In the present study, ANSYS16 (Mechanical APDL) multiphysics finite element software was utilized to construct and perform numerical linear simulations on the designed structures in order to analyze their Poisson's ratio and Young's modulus. The structures were meshed using BEAM189 elements with a rectangular cross-section. The systems were

Table 1
The values of different parameters.

Parameters	Value (mm)
i	24
j	1.2, 2.4, 3.6, …, 84
k	1.2, 2.4, 3.6, …, 84
t	0.1
d	1.0

simulated as single representative unit cells (RUCs) under general periodic boundary conditions. The size of the rectangular RUC, defined by the lengths L_x and L_y (shown in Fig. 5), may be found as a function of the parameters i, j and k as follows [50]:

$$L_x = \sqrt{i^2+k^2-2ik\cos\left(\arccos\left(\frac{i^2+k^2-j^2}{2ik}\right)+\frac{\pi}{3}\right)} + \sqrt{i^2+j^2-2ij\cos\left(\arccos\left(\frac{i^2+j^2-k^2}{2ij}\right)+\frac{\pi}{3}\right)} + \sqrt{j^2+k^2-2jk\cos\left(\arccos\left(\frac{j^2+k^2-i^2}{2jk}\right)+\frac{\pi}{3}\right)} \tag{6}$$

$$L_y = L_x\tan\left(\frac{\pi}{6}\right) \tag{7}$$

Following convergence testing, the element size was set as i/120 to ensure that there are at least six elements in the smallest possible length of ligament in the most extreme cases of the hexagonal tessellation, i.e. when j or k are equal to 0.05(i). The BEAM189 element is based on Timoshenko beam theory, which takes into account shear deformation effects and is suitable for analyzing slender to moderately thick beam structures. The element is a quadratic three-node beam, with default

settings providing six degrees of freedom at each node, including three translations and three rotations [51]. The constitutive material properties were set to those of linear isotropic Onyx® Nylon [52], with the Young's modulus and Poisson's ratio defined as $E = 1$ GPa and $\nu = 0.3$, respectively.

2.3. Implementation of periodic boundary conditions and Loading of Systems

Following the selection of the appropriate RUC, the next step involves applying periodic boundary conditions (PBCs) to the system. The metamaterial geometry examined in this study lacks an axis of mirror symmetry and, consequently, PBCs must be implemented through the use of specific constraint equations on the unit cell's boundary nodes. The constraint equations correlate the displacement and rotation of nodes on one edge of the rectangular unit cell to those on the opposite edge. In this work, a modified version of the methodology presented in [53] was employed, with the key distinction that BEAM elements were used in our implementation in the linear parametric FE simulations. Since BEAM elements possess six degrees of freedom (three displacements and three rotational degrees of freedom) as opposed to traditional plane and brick/tetrahedral elements, which possess two and three displacement-linked degrees of freedom only, respectively, the boundary conditions were imposed in the following manner:

First, the nodes at each pair of horizontal and vertical edges (*xy*-plane) were bound to each other through Eqs. (8)–(11) in order to ensure that the deformation on one edge is mirrored on the corresponding opposing side. The following constraint equations were used:

$$Ux_{1,Master} - Ux_{2,Master} - Ux_{1,Slave} + Ux_{2,Slave} = 0 \tag{8}$$

$$Uy_{1,Master} - Uy_{2,Master} - Uy_{1,Slave} + Uy_{2,Slave} = 0 \tag{9}$$

$$(ROT)z_1 = (ROT)z_2 \tag{10}$$

Where Ux_i and Uy_i denote displacements in the x and y-directions respectively, and $ROTz_i$ indicates the rotational degree of freedom normal to the z-axis. The numbers 1 and 2 indicate the two sides in a pair of opposing edges. In the case of the displacement boundary conditions, two pairs nodes are also denoted as "master" nodes and the paired displacement of these nodes is mirrored by the "slave" nodes (see Fig. 6) which correspond to all other paired nodes on the same edges (Eqs. (8) and (9)). Individual constraint equations pair each set of slave nodes to the master nodes. Further details on this methodology may be found in [53]. In the case of the rotational degrees of freedom, the only constraint involves pairing two opposing nodes (Eq. (10)).

Since the simulated systems are 2D structures, planarity is imposed by blocking the remaining degrees of freedom. Consequently, the following constraints through Eqs. (11)–(13) should be applied to all of the nodes:

$$U_Z = 0 \tag{11}$$

$$(ROT)_x = 0 \tag{12}$$

$$(ROT)_y = 0 \tag{13}$$

Following the establishment of the PBCs and the planarity conditions, the system needs to be fixed to ensure that does not undergo rigid body motion upon loading. In view of this, the system was fixed from one node on the bottom edge (as shown in Fig. 6) in the x and y-directions, while the corresponding node in the upper edge was blocked in the x-direction only. This ensures that the RUC remains aligned with the y-axis during deforming while allowing the overall structure to deform freely, even undergoing non-orthotropic deformations if necessary.

Each system was subjected to on-axis unidirectional tensile loading in the x and y directions individually in order to evaluate the mechanical properties. This was carried out through the application of a force of 10 N distributed evenly across the number of nodes at the edges of the RUC and applied separately in both the x and y directions.

It's worth noting that, at this stage, we employed a beam element model for the RUCs in order to perform a large number of linear parametric FE simulations. The choice of simulating RUCs with beam elements offers a computationally efficient approach that enables us to efficiently explore the Poisson's ratios and Young's moduli of a very wide range of hexagonal tessellations. Following this investigation, we identified promising structures based on the parametric simulation results, which were representative of the full range of Poisson's ratio values and we transitioned to a more accurate non-linear modeling approach using the PLANE183 element for these specific cases as detailed in the next section.

2.4. Experimental tests and non-linear finite element simulations

As mentioned previously, in order to validate the simulation results, three samples representative of configurations with the largest negative, zero, and highest positive Poisson's ratios were fabricated and tested. The length combinations (i, j, k) for each hexagonal unit in these prototypes were determined based on linear FE simulation results and are presented in Table 2. As shown in Fig. 7(a–c), the printed prototypes comprise a 3 × 5 RUC system (i.e., 3 RUCs in the horizontal direction

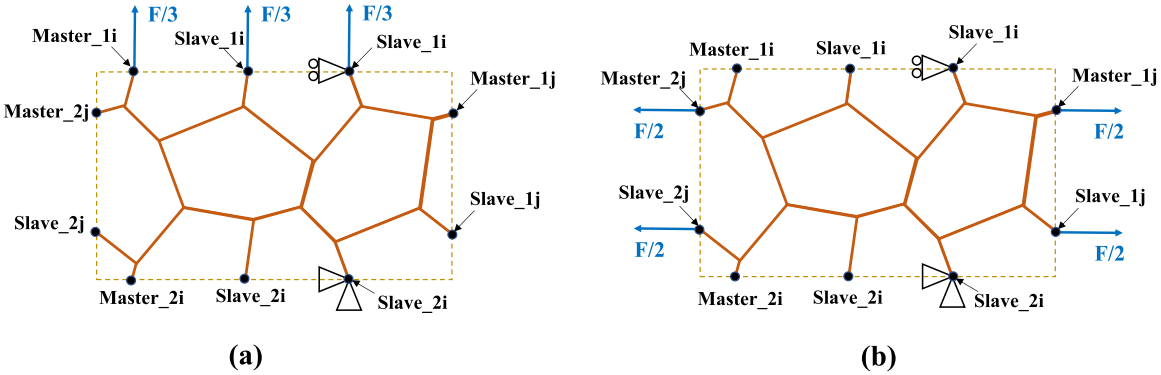

Fig. 6. Constraints include a fixed node at the bottom in both the x- and y-directions, as well as blocking the corresponding node at the top edge in just the x-direction, along with the loading conditions applied on the unit cell: a) loading on the y-direction and b) loading on the x-direction. The sets of master and slave nodes on the topmost, bottommost, rightmost and leftmost edges are indicated. The top edge nodes, which are denoted as Master_1i and Slave_1i are paired with the bottom edge nodes, denoted as Master_2i and Slave_2i, through constraint equations. Similarly, the rightmost edge nodes, labelled Master_1j and Slave_1j, are paired with the leftmost edge nodes labelled Master_2j and Slave_2j. Further details on this methodology may be found in [53].

Table 2
Geometry of additively manufactured prototypes with 3 × 5 RUC system.

Sample name	i (mm)	j (mm)	k (mm)	Horizontal length, L_x (mm)	Vertical length, L_y (mm)
I	24	16	8	190.49	183.3
II	24	12	12	187.06	180
III	21	17.6	7.4	223.81	215.36

and 5 RUCs in the vertical direction) with rectangular blocks of material, each 10 mm in height, added to the uppermost and lowermost edges to facilitate sample placement in the tensile loading machine and improve load distribution on the samples. All prototypes were designed with an in-plane ligament thickness of 1 mm and a constant out-of-plane thickness of 30 mm. They were then manufactured using a Markforged® 3D printing machine with Onyx® Nylon material.

Prior to testing, all the additively manufactured samples were painted with a black-and-white speckle pattern for Digital Image Correlation (DIC) to measure the Poisson's ratio and analyse the deformation behaviour of these systems. These prepared samples were subsequently tested under small-strain compressive loading using a Galdabini® universal tensile machine equipped with a 50 N load cell at a speed of 5 mm/min (see Fig. 7d). The Poisson's ratio of the central RUC of each structure was measured during the deformation process using DIC analysis (see Fig. 7e). This was achieved by tracking the four corners of the central RUC in each image and subsequently calculating the strain and Poisson's ratio for consecutive steps. In this methodology the average lengths of the central unit cell in both principal directions (L_x and L_y) are first measured from the initial image. Then, the strain in both directions and the corresponding Poisson's ratio at each stage are determined using the variations of these two values at each stage relative to the first stage.

In addition to conducting experimental compression tests, non-linear geometric simulations using the PLANE183 element were also carried

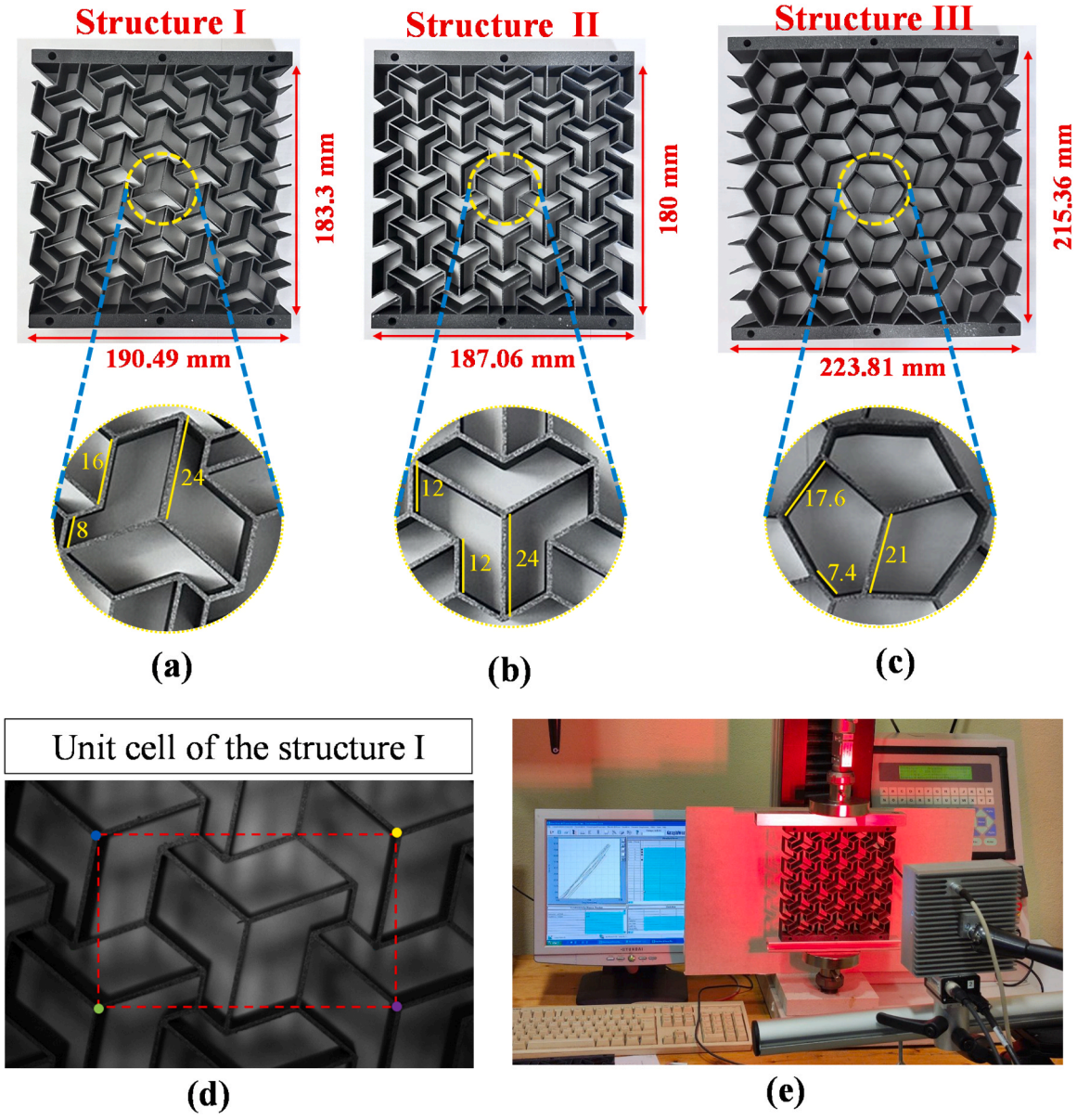

Fig. 7. AM prototypes representing structures, along with the configuration of the compression test setup: a) hexagonal structure representative of the zero Poisson's ratio (Structure I); b) hexagonal structure representative of the most negative Poisson's ratio (Structure II), c) hexagonal structure representative of the most positive Poisson's ratio (Structure III); d) Structure I showing the central unit cell and the points used to measure the Poisson's ratio of the system with DIC; and e) image showing the setup used for the compression tests.

out on the RUC of these three structures in order to compare the deformation mechanism and analyse any geometric nonlinearities which may arise during loading. This was done since PLANE elements, which are two-dimensional plane-stress elements can capture more accurately the stress distributions within the system, particularly at the interconnection regions and allow for a more precise comparison with the experimental results. The simulations were carried out under PBCs, analogous to those employed for the beam element simulations (shown in Fig. 6), to the RUC of each structure, along with a small-strain compressive loading system of up to 5 % globally in the *y*-direction, using small increments. The Poisson's ratio of the system was extracted for each substep and compared with the experimental values obtained through the DIC evaluation for each of the three additively-manufactured prototypes.

3. Results and discussion

In this section, the results of the parametric FE simulation analysis and the experimental tests are presented. Both the individual results and the comparison between the numerical and experimental results are discussed in detail. Since these systems possess trigonal in-plane rotational symmetry, they exhibit transverse isotropy [54,55] (as confirmed by the results obtained, which were always identical for loading the x- and y-directions) and thus the results for each geometric configuration are reported in terms of a single Poisson's ratio and Young's modulus.

3.1. Linear finite element simulation

a) Poisson's Ratio

The 3D and 2D scatter plots of FE results obtained for the Poisson's ratio (ν) of the defined structures versus j/i and k/i are presented in Fig. 8. As stated previously, i was fixed at a constant value equal to 24 mm throughout the parametric simulation run, whereas the values for j and k were varied in the range of $0.05i$ to $3.5i$ (1.2 mm to 84 mm).

As one can observe in Fig. 8a, most of the designed structures have indicated a Poisson's ratio of more or less + 1; however, there are a select number of structures that have the potential to exhibit a wide range of values incorporating positive, negative, and zero Poisson's ratios.

The 2D plots of Poisson's ratios versus j/i and k/i, which are projections of the 3D plot on the j/i and k/i planes, are depicted in Fig. 8b and c, respectively. As one can observe in Fig. 8b and c, the variation of Poisson's ratio for both projections is exactly the same, which verifies the symmetrical behaviour of the system to the plane $j/i = k/i$.

The majority of configurations, as shown in Figs. 8 and 9, exhibit a Poisson's ratio $+0.99 \leq \nu < +1$. This includes all convex configurations and a large proportion of concave structures. However, it is also evident that solely for configurations which pertain to one of the following geometric conditions:$j = i + k$, $k = i + j$ and $i = j + k$, the Poisson's ratio varies considerably. A visual analysis of the deformation mechanism indicates that there is a change in deformation modes at these boundary configurations with respect to the other structures. It appears as though re-entrant arrowhead-like deformations [56] are occurring in the systems exhibiting negative Poisson's ratio while the other systems deform similarly to typical hexagonal cellular honeycombs [43], which exhibit a Poisson's ratio of near + 1. In Fig. 8b,c and Fig. 9b,c, projections for the boundary configurations are shown. The Poisson's ratios for all of the designed structures vary from nearly −0.22 to approximately + 1. These specific cases all involve concave configurations and their mechanical properties differ considerably from the other concave structures in which these conditions are not met.

As one may observe from Fig. 9c, two concave hexagons with zero Poisson's ratio (ZPR) can be seen on the boundary line $i = j + k$, which are indicated by red circles. The j values for these structures with ZPR are 8 and 16, and the combinations of these two points are $i = 24$, $j = 8$, and $k = 16$, and $i = 24$, $j = 16$, and $k = 8$, respectively. The Poisson's ratio decreases in the region between these two points and becomes negative down to a minimum Poisson's ratio (MPR) of −0.2217 on the midpoint. This point corresponds to the following configuration $i = 24$,

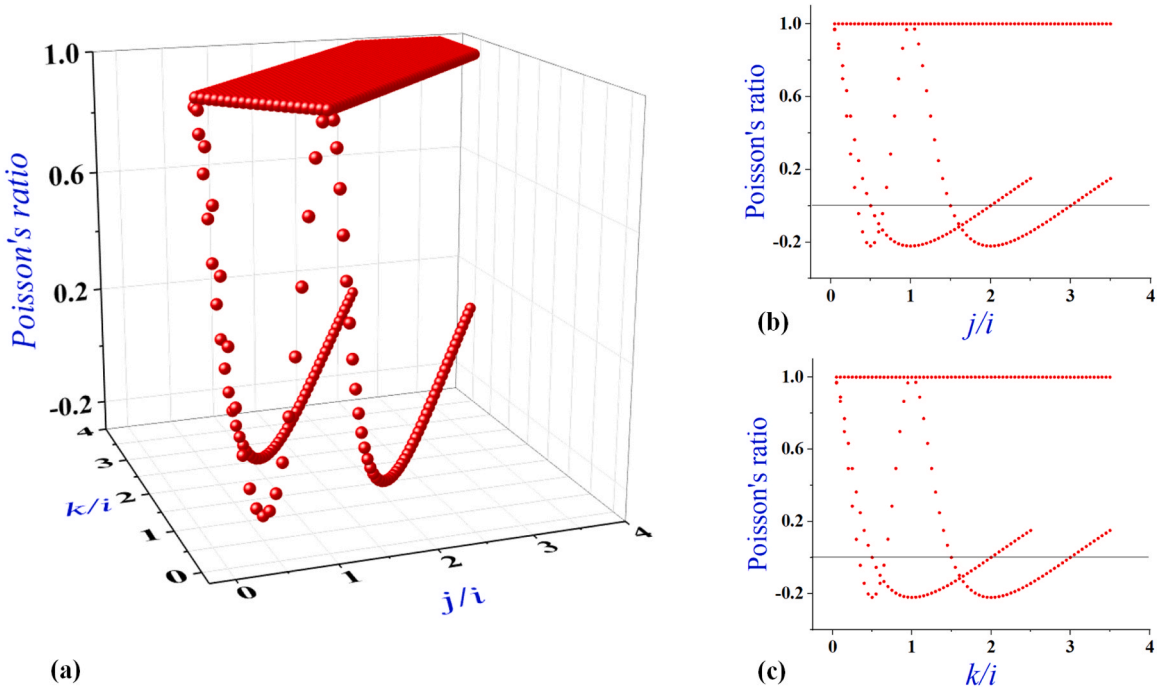

Fig. 8. The scatter plot of FE results obtained for the Poisson's ratio of the whole designed structures: a) 3D plot of Poisson's ratio versus k/i and j/i while keeping i as a constant value of 24; b) and c) 2D plot of Poisson's ratio versus j/i and k/i, respectively, which extracted from projections of the 3D plot on the planes Poisson's ratio-j/i and Poisson's ratio-k/i, respectively, to verify the symmetrical behaviour of the system to the plane j/i = k/i as well as the range of Poisson's ratio more clearly.

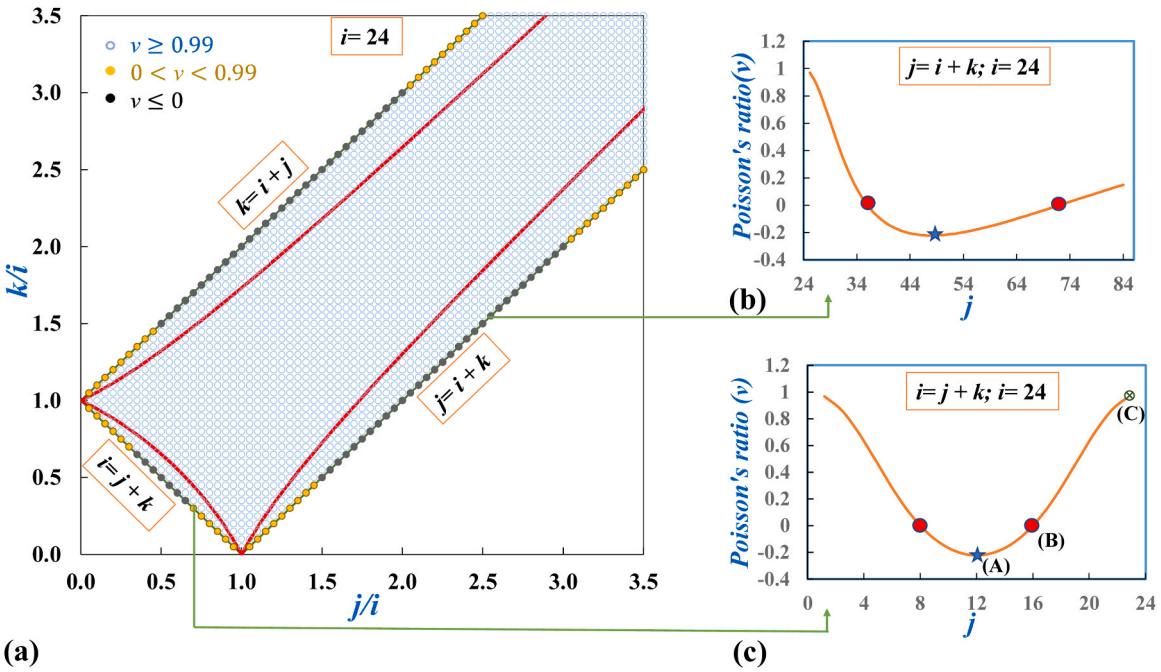

Fig. 9. The contour plot of Poisson's ratio versus j/i and k/i as well as the variation of Poisson's ratio on the boundary areas; a) Mapping of the values of Poisson's ratio (v) extracted from FE simulation on the theoretical realizable (convex or concave shown by the red lines) area by considering i = 24 and dividing the values into three different categories, i.e., Poisson's ratio greater than or equals to 0.99 (light blue area), between zero and 0.99 (orange circles), and less than or equals to zero (black circles); b) the variation of Poisson's ratio for the structures with i = 24 and j = i + k (24 < j < 84); and c) the variation of Poisson's ratio for the structures with i = 24 and i = j + k (j < 24). The red circles indicate the points where the Poisson's ratio changes from positive to negative (and vice-versa) while the star indicates the minimum Poisson's ratio obtained (v = −0.22).

$j = 12$, and $k = 12$. Furthermore, the Poisson's ratio gradually increases by moving away from each of those two points ($j = 8$ and 16). The maximum Poisson's ratio of around + 0.96 was found at the extremities of the line at the following configurations: $i = 24$, $j = 1.2$, and $k = 22.8$, and $i = 24$, $j = 22.8$, and $k = 1.2$. It is worth noting that the plot (see Fig. 9c) is symmetric since geometrically identical structures are formed due to the presence of same i value and interchangeable j and k values.

Similarly, for boundary line$j = i + k$ shown in Fig. 9b, a similar scenario can be found. In this case, the combinations of $i = 24$, $j = 36$, and $k = 12$, and $i = 24$, $j = 72$, and $k = 48$, are the two configurations that resulted in concave structures with ZPR (marked by the red circles). Similarly, the minimum negative Poisson's ratio obtained is –0.2217 for the combination: of $i = 24$, $j = 48$, and $k = 24$. The Poisson's ratio is also positive at the extremities of the plot. It is worth noting that in this case, the plot is not symmetric since the equation$j = i + k$ has no bounds in one direction unlike the equation $i = j + k$ which is bounded on both ends.

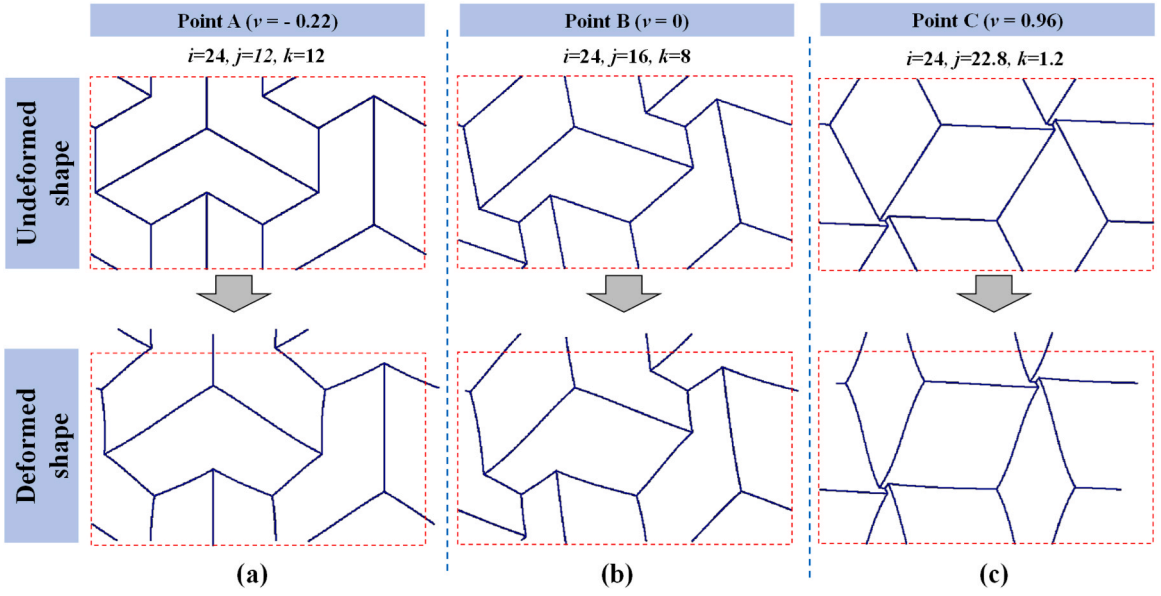

Fig. 10. The undeformed and deformed shapes of three different configurations for loading in the y-direction which are indicated by point A, B and C in Fig. 8c; a) Point A with minimum Poisson's ratio of −0.2217, b) Point B with zero Poisson's ratio, and c) Point C with positive Poisson's ratio. The deformed structures are magnified through displacement scaling to 10 % strain in the y-direction.

For the third boundary line, $k = i + j$, the trends are exactly identical to the boundary line $j = i + k$ because of the symmetry feature.

The undeformed and deformed shapes under tensile loading in the *y*-direction for the combinations pertaining to points A, B, and C (see Fig. 9c) representing different Poisson's ratios are illustrated in Fig. 10. In the case of the negative Poisson ratio system shown in Fig. 10a, the auxeticity appears to arise from re-entrant deformation modes. On the other hand, in the highly positive Poisson ratio system (Fig. 10c), the tessellation appears to degenerate into a rhombile tiling (a quadrilateral-based tessellation [49,57]) due to one set of sides becoming extremely small relative to the other two. This tessellation is known in the literature to exhibit a highly positive Poisson's ratio [46].

Given the specific nature of the combinations which give rise to zero and negative Poisson's ratios observed in the numerical simulation run, it is possible to extract mathematical relationships to predict which set of variables may be used to obtain these properties. A generic schematic plot of k/i versus j/i is depicted in Fig. 11, where the combinations which give rise to ZPR and MPR are indicated with red circles and blue stars, respectively. In Table 3, the equations which give rise to these values are listed. These equations are expressed in terms of ratios, meaning that they can apply to configurations which go beyond the set of combinations evaluated in this parametric simulation run.

These equations demonstrate that:

i. There are six combinations for the lengths: *i*, *j* and *k* which can results in ZPR listed in Table 3.
ii. There are 3 combinations for the lengths: which can result in MPR ($\nu = -0.2217$) listed in Table 3.

b) Young's Modulus

The 3D scatter plot and the contour plot of FE results obtained for effective Young's modulus of all defined structures (considering the externally formed triangle) versus j/i and k/i are depicted in Fig. 12. The effective Young's modulus (E^*) of each structure is calculated by dividing its Young's modulus (E_{meta}), obtained from the FE simulation, by the predefined Young's modulus of the material (E_{mat}), which is

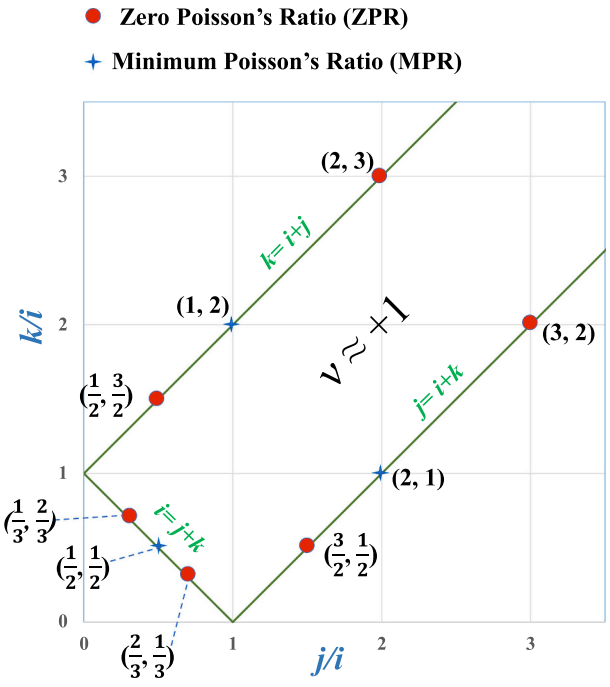

Fig. 11. A schematic plot of k/i vs. j/i to point out the combinations of i, j, and k with ZPR and MPR, which are located on the three boundary lines (concave structures) dividing realizable and unrealizable areas.

Table 3
Combinations of i, j, and k exhibiting ZPR and MPR by considering i as a constant value. For each combination, an example with i = 24 is presented.

First condition	Second condition	*i*	*j*	*k*	ZPR or MPR
$i = j + k$	$j = 2i/3;\ k = i/3$	24	16	8	ZPR
	$j = i/3;\ k = 2i/3$	24	8	16	ZPR
	$j = k = i/2$	24	12	12	MPR
$j = i + k$	$j = 3i/2;\ k = i/2$	24	36	12	ZPR
	$j = 3i;\ k = 2i$	24	72	48	ZPR
	$k = i = j/2$	24	48	24	MPR
$k = i + j$	$j = i/2;\ k = 3i/2$	24	12	36	ZPR
	$j = 2i;\ k = 3i$	24	48	72	ZPR
	$i = j = k/2$	24	24	48	MPR

1 GPa. Therefore, this dimensionless parameter can be defined as follows:

$$E^* = \frac{E_{meta}}{E_{mat}} \tag{14}$$

As can be seen in Fig. 12a, the symmetrical behaviour observed for the Poisson's ratio regarding the plane $j/i = k/i$ is also evident here. Moreover, the anomalous cases shown previously for the Poisson's ratio are also observed for the Young's modulus. As shown in Fig. 12a, three curvature lines are distinctly separated from the other results.

The maximum effective Young's modulus can be found in the region around $k/i = 0.55$, $j/i = 0.5$ and vice-versa at a value of 469×10^{-9}as shown in Fig. 12b, while the minimum value is found at $j/i = 2.5$, $k/i = 3.5$ and *vice-versa* at a value of 6.08×10^{-9}. This variation is probably related to the deformation mechanisms, mentioned previously, which resulted in different Poisson's ratios as well as beam theory considerations relating to the different ligament lengths found in the various configurations (i.e. the presence of extremely long, thin beams results in weak structures in comparison to systems with shorter ligaments).

The peculiar variations of effective Young's modulus for the combinations on the boundary lines $i = j + k$ and $j = i + k$ are depicted in Fig. 12c and d, respectively. On the line $i = j + k$(see Fig. 12c), the minimum effective Young's modulus is located in the central point, where $j/i = k/i = 0.5$ while the effective Young's modulus increases as one approaches the boundaries. On the line $j = i + k$(see Fig. 12d), a decreasing trend can be seen by increasing the variables *j* and *k*, tending towards a minimum as these ligament lengths increase. These trends are all in line with expectations, since they indicate that systems with short ligament lengths are considerably stiffer than those with longer ligaments which is in accordance with standard beam mechanics.

It is important to note that the values shown in Fig. 12, which at first glance appear to be extremely low in magnitude, are conditioned by the fact that a very thin in-plane ligament thickness value was utilized (0.1 mm) for the simulations. For systems with sufficiently long ligaments (Euler-Bernoulli beams), thicker ligaments may be used to considerably enhance the overall effective Young's modulus whilst retaining the same deformation mechanism and Poisson's ratio.

c) Two different concave hexagons with the same side lengths

As discussed previously in Section 2.1, a small number of particular combinations of variables can result in concave hexagonal tessellations that can manifest in two distinct geometrical configurations: one where isosceles triangles are positioned externally and another where they are positioned internally relative to the central triangle (see Fig. 13b and c). The mathematical rules governing which combinations of the variables *i*, *j*, and *k* have the ability to present these two different concave configurations are addressed in Appendix 1.

These systems represent an extremely small subset of the design space of these hexagonal tessellations, shown in Fig. 13a in the blue shaded section. A small number of these structures; a series of variable

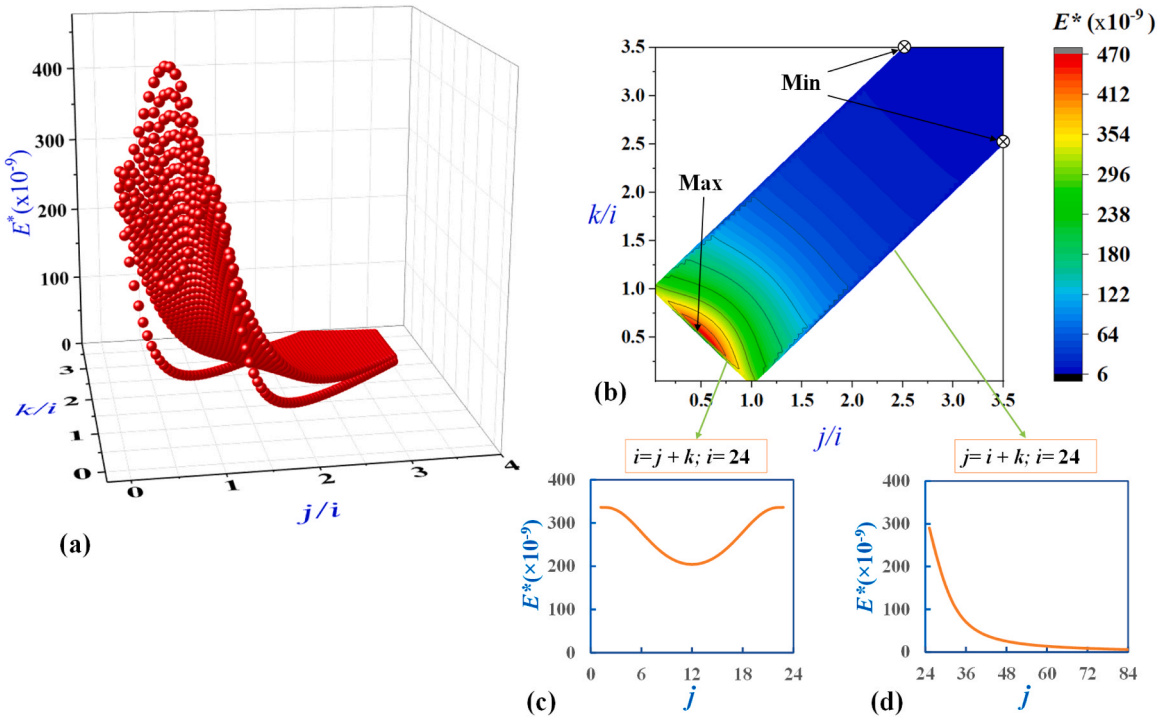

Fig. 12. The 3D scatter plot and contour plot of FE results obtained for the effective Young's modulus of the entire set of structures by considering externally formed triangle and i = 24: a) 3D plot of the effective Young's modulus versus k/i and j/i; b) The contour plot of effective Young's modulus (E*) versus j/i and k/i; c) the variation of effective Young's modulus for the structures with i = 24 and i = j + k (j < 24); and d) the variation of effective Young's modulus for the structures with i = 24 and j = i + k (24 < j < 84).

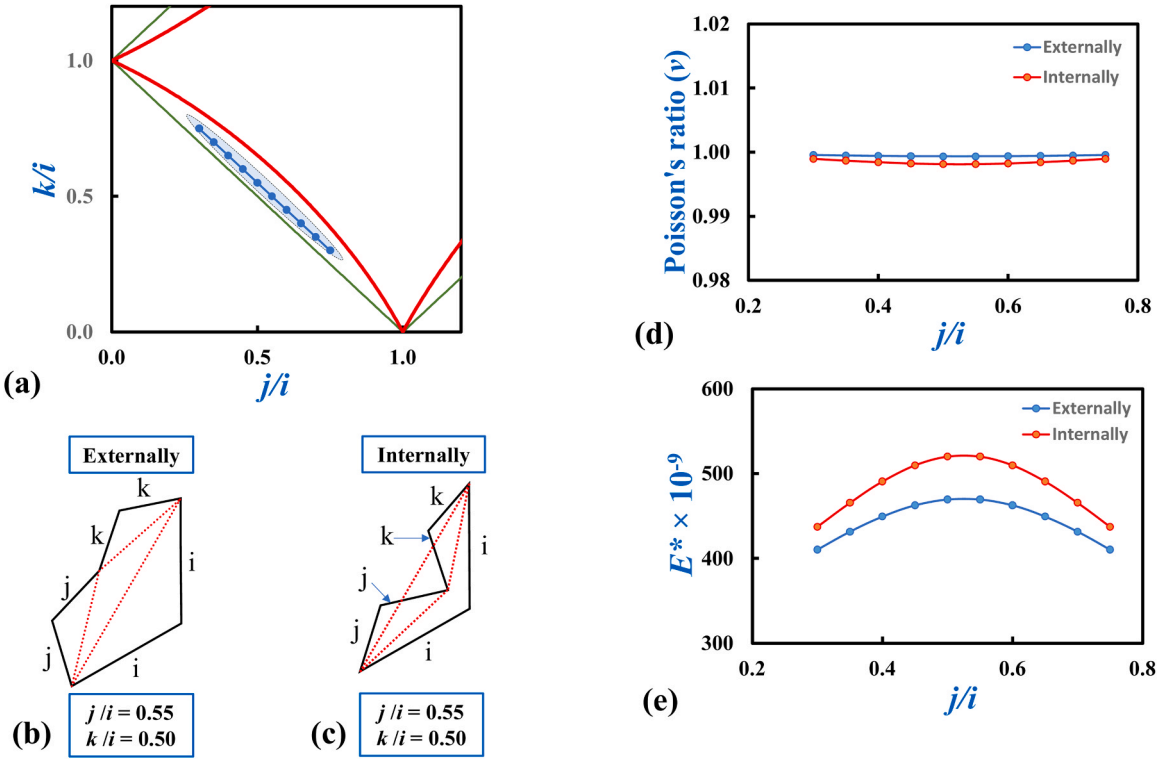

Fig. 13. The comparison of the Poisson's ratio and effective Young's modulus for a series of specified variable combinations capable of forming both externally and internally concave hexagonal configurations: a) the location of the selected combinations along the line j + k = 1.05i; b) a schematic illustrating the concept of external and internal configurations; c, d) the comparison of the Poisson's ratio and effective Young's modulus of the considered combinations, respectively.

combinations along the line $j + k = 1.05i$ (see Fig. 13a); were simulated and compared with the "normal" external triangle corresponding hexagonal systems. It is evident from the plot in Fig. 13d that the Poisson's ratios for both configurations are nearly identical at *ca.* $+1$. This is congruent with the findings presented in the previous sections which showed that all configurations which are not on border of the realizability condition (Eq. (2)) exhibit a highly positive Poisson's ratio. In the case of the Young's modulus, some slight differences were observed between the two corresponding systems as the internally formed triangle systems are marginally stiffer in comparison to the externally formed systems (see Fig. 13e). As the selected structures (see Fig. 13a) represent the maximum Young's moduli when considering externally formed triangles (see Fig. 12a and b), and the Young's moduli for their corresponding structures with internally formed triangles are higher than those of the former, the maximum Young's modulus—considering both internally and externally contained triangles—corresponds to the internally formed ones, as depicted in Fig. 13e. This is most probably due to the fact that the former systems have a more compact unit cell with a smaller area than the latter. All of this indicates that this small subset of systems with identical dimensions but two distinct realizeable geometries exhibit very small differences from a mechanical point of view.

3.2. Experimental and non-linear finite element simulations

As stated previously, three configurations representative of systems exhibiting a positive, zero and negative Poisson's ratio were realized through additive-manufacturing and experimentally tested. Fig. 14 shows the deformation behavior (a–c) and a comparative analysis of the Poisson's ratio (d) as a function of axial strain of these three distinct structures, labeled I, II, and III, under quasi-static small-strain (up to 5 %) compressive loading. It is evident that the deformation behavior of all three systems under experimental tests is similar to their predicted FEM simulations. Moreover, the results obtained from the experimental tests generally demonstrate an extremely good level of similarity to those derived from nonlinear periodic simulations for all three structures.

For Structure I, the Poisson's ratios of both the experimental and simulation data exhibit a similar nearly-constant value of zero. The experimental results show an initial value of almost zero, which

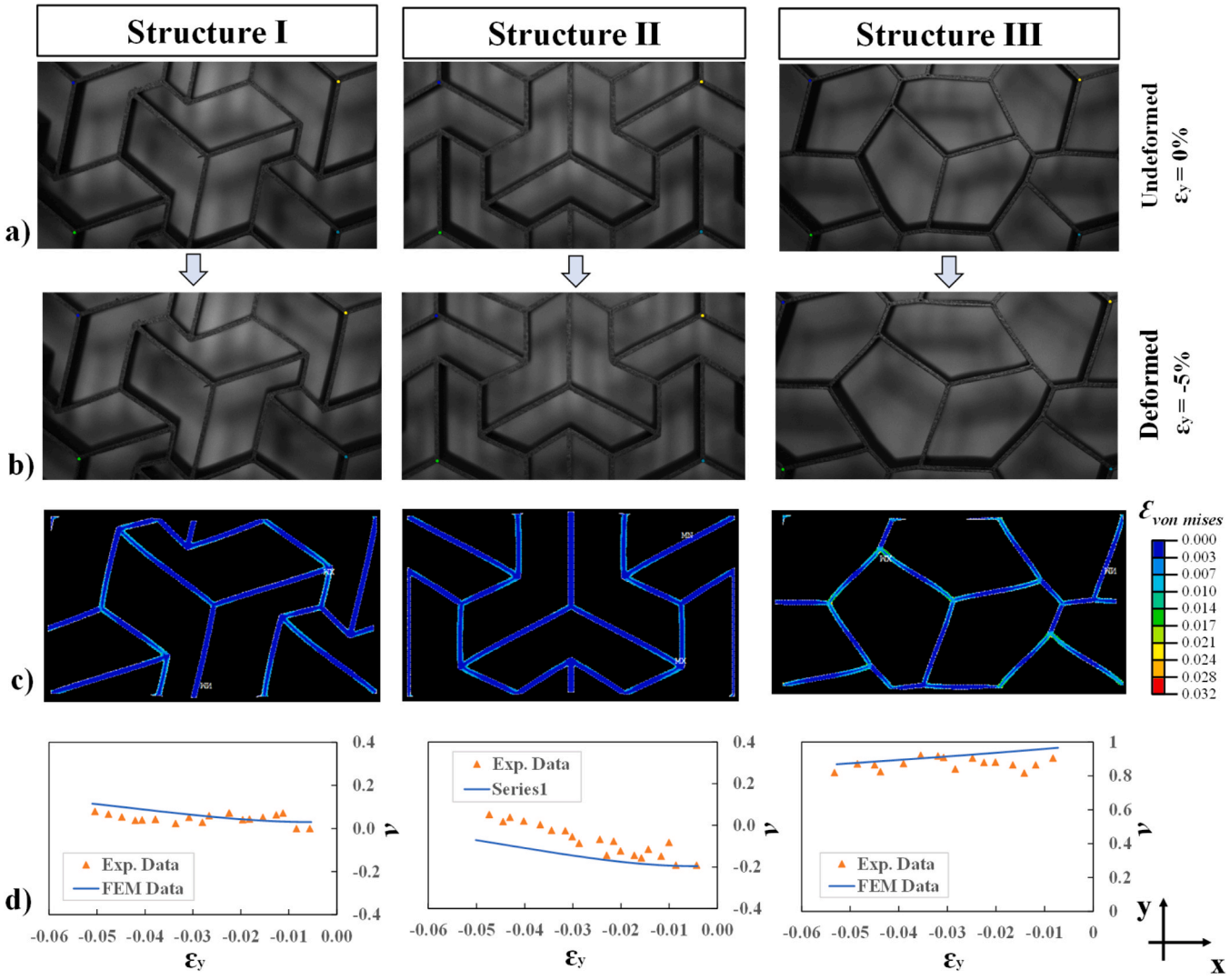

Fig. 14. Images representing (a) undeformed and (b) deformed additively manufactured prototypes labeled structure I, II and III subjected to ca. 5 % compressive engineering strain. In each of these images a set of four different colors placed on the corners of central rectangular RUC from which the Poisson's ratios and engineering strains of the systems were measured using DIC images. Images set (c) represents the FEM simulations and the elastic von Mises strain obtained for the RUC of all the systems. Plots in set (d) show a comparison of engineering Poisson's ratio obtained from experimental tests and FEM geometric nonlinear simulations versus engineering strain subjected to the central RUC.

gradually increases up to + 0.08 at 5 % compressive strain. This behaviour is mirrored in the nonlinear simulations where the Poisson's ratio slowly rises from an initial value of + 0.03 (almost zero in practical terms) up to + 0.11 as the transverse strain reaches 5 %. In the case of Structure II, which was predicted by the linear FE simulations to exhibit a slightly negative Poisson's ratio, the auxeticity of the system was confirmed by the experimental results at small strain ranges. As shown in Fig. 14d, the system was experimentally shown to initially exhibit a Poisson's ratio of −0.19 which gradually decreases in magnitude as the compressive strain increases up to a value of ca. zero at 5 % strain. The nonlinear FE simulations predicted a similar behaviour, with the Poisson's ratio starting at −0.19 before gradually decreasing to −0.07 over the same strain range. This gradual transition towards a positive Poisson's ratio, which is primarily attributed to the change of configuration induced by geometric nonlinearities, means that this geometry is only auxetic over a limited strain range. Finally, Structure III shows a Poisson's ratio of nearly + 1, as predicted by the linear FE simulations. This Poisson's ratio value gradually decreases as compressive strain increases, with both FEM and experimental data following this pattern. Specifically, from the FEM results, the Poisson's ratio starts at + 0.96 and decreases to + 0.86 at a strain of around 0.05, while the corresponding data from the experimental tests are + 0.90 and + 0.82, respectively. This indicates that this structure exhibits a highly positive Poisson's ratio under small-strain conditions, as predicted.

Before concluding, it is important to highlight the significance of this work. These hexagonal tessellations represent a class of isotropic metamaterials with trigonal rotational symmetry; a characteristic which is rarely found in other auxetic metamaterial structures. This property is retained for all configurations studied in this work, and as demonstrated by the FE simulations and experimental tests, these tessellations exhibit significant versatility, with a Poisson's ratio ranging from + 1 to – 0.22 and a wide spectrum of effective stiffnesses, tailored as a function of geometric parameters. It is important to note that the mechanical properties of these systems are defined by the ratios between the hexagonal dimensions, *i*, *j* and *k* and the thickness of the ligaments, t, and not by the absolute values of these variables and thus, in this work, we considered almost the entire spectrum of permissible geometries for this tessellation. It is also worth highlighting that this class of hexagonal tessellation is merely one of many which may be formed whilst retaining the rotational trigonal symmetry characteristic (and, hence, the transverse isotropy) and that a number of derivative tessellations may also be formed on the basis of the system presented in this work. This is expected to considerably widen the potential range of mechanical properties (including Poisson's ratios) which may be obtained from these tessellations and it is envisaged that this work can act as blueprint for the design of further mechanical metamaterials based on Euclidean polygonal tessellations.

4. Conclusion

In this study, we have proposed a new class of mechanical metamaterials based on hexagonal tessellations with trigonal rotational symmetry. Geometric expressions pertaining to the realizability and concavity of these tessellations were derived and the Poisson's ratios and Young's moduli of various geometric configurations were investigated. These systems were shown to exhibit a wide range of Poisson's ratios, from highly positive to small auxetic values whilst retaining their transverse isotropy. The effect of geometry on the mechanical properties of these systems was studied through a wide ranging parametric FEM simulation run and three additively-manufactured prototypes, representative of the entire Poisson's ratio range (i.e. negative, zero and positive Poisson's ratio) were experimentally tested and analysed using DIC. The results obtained from the experimental tests tallied extremely well with the FE predictions and confirm the results obtained from the initial parametric simulation run. The main findings of this work can be summarized as follows:

- These hexagonal tessellations have the ability to exhibit Poisson's ratios ranging from approximately −0.2 to + 1 as well as a wide spectrum of Young's moduli.
- The Poisson's ratios for all the combinations located inside the realizable area, including both concave and convex hexagons, were approximately + 1, while the Poisson's ratios for the hexagonal structures whose combinations are located on the boundary line between the realizable and unrealizable areas can be negative, zero, or positive.
- The geometric configurations which give rise to the minimum (i.e. most auxetic) and zero Poisson's ratios were identified along with the systems possessing the maximum and minimum Young's moduli.
- The quasi-static small-strain compressive tests on the additively-manufactured prototypes verified the results obtained from the FEM simulations.

CRediT authorship contribution statement

Reza Moghimimonfared: Writing – original draft, Methodology, Investigation, Formal analysis, Data curation, Conceptualization. **Andrea Spaggiari:** Validation, Supervision, Methodology. **Luigi Grasselli:** Validation, Methodology. **Luke Mizzi:** Writing – review & editing, Validation, Supervision, Funding acquisition, Conceptualization.

Declaration of Competing Interest

The authors declare that they have no known competing financial interests or personal relationships that could have appeared to influence the work reported in this paper.

Acknowledgements

This work was carried out within the framework of the project "A fundamental understanding of disorder in metamaterials," funded by Fondazione Cariplo and Fondazione CDP, grant no: 2023-2526, supporting young Italian researchers in ERC competitions.

Appendix 1. Geometric conditions for availability of internal triangle

In this section, the geometric conditions for the realization of particular concave hexagons for which two distinct geometrical configurations can be identified for systems with the same side lengths *i*, *j*, and *k* are listed. These two configurations are classified as externally and internally triangle-contained configurations and schematics representing these two types of concave hexagons are illustrated in Fig. 13b and c.

In order to determine whether a chosen combination of *i*, *j* and *k*, which respects the geometric limits defined in Eqs. (1) and (2) and the concavity conditions listed in Eq. (3)–(5), can possess one or two realizable configurations, the following steps must be taken. First, two circles are drawn with the centre on the vertices of the base of the isosceles triangle formed by two longest sides. Considering Fig. A1 as an example, the sides with length *i* are longer than *j* and *k*, and therefore, the circles are drawn with centre points at vertices A and C. If, the sides *j* or *k* were the longest, the circles would have been drawn on vertices A and E or C and E, respectively.

The circle centred at the vertex where the side with length *i* meets the side with length *k* (Point C) has a radius of $k\sqrt{3}$, while the second circle

centered at Point A, (where the side with length j meets the side with length i) has a radius of $j\sqrt{3}$. These two circles intersect each other at two points, E and P. As shown in Fig. A1, if point P is found inside the hexagonal tiling then two configurations are realizable (b). Elsewise, only one configuration can exist (a).

In order to express these considerations in mathematical terms (see Fig. A1), we can state that:

a. One configuration is realizable if the length MP is greater than or equal to the length MN
b. Two configurations are realizable if the length MP is less than the length MN

The length MP is defined as the distance between points M and P, where P is one of the intersections of the two circles and M is the midpoint of the line formed between the two intersections of the circles. The length MN is the distance between points M and N, with the latter, N, being defined as the point where the line between the two intersections of the circles intersects with the longest side of the hexagonal tiling (in the case shown in Fig. A1b, side i). These two lengths can be defined in terms of the original parameters: i, j and k, as follows:

$$MP = \left(k\sqrt{3}\right)\sin\theta \tag{A1}$$

$$MN = k\cos\theta \tag{A2}$$

Where θ is defined as follows:

$$\theta = \arccos\left(\frac{i^2 + k^2 - j^2}{2ik}\right) \tag{A3}$$

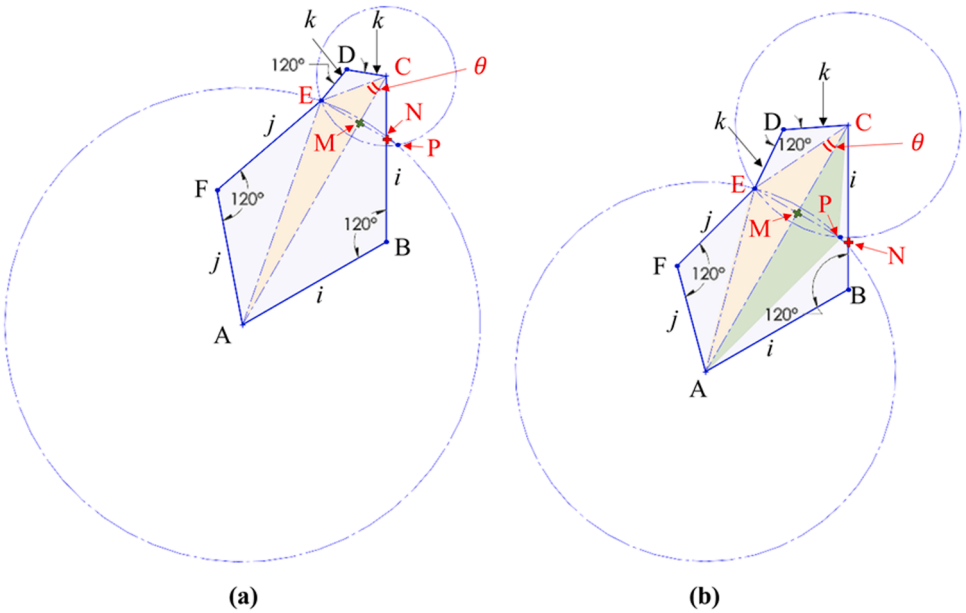

Fig. A1. The geometric schematics represent two different types of concave hexagons, distinguished by the presence or absence of internally contained configurations: a) concave hexagon capable of presenting only external configuration, and b) concave hexagon capable of presenting both external and internal configurations

Data availability

Data will be made available on request.

References

[1] K. Bertoldi, V. Vitelli, J. Christensen, et al., Flexible mechanical metamaterials, Nat. Rev. Mater. 2 (2017) 17066.
[2] X. Ren, R. Das, P. Tran, et al., Auxetic metamaterials and structures: a review, Smart Mater. Struct. 27 (2018) 023001.
[3] X. Yu, J. Zhou, H. Liang, et al., Mechanical metamaterials associated with stiffness, rigidity and compressibility: a brief review, Prog. Mater. Sci. 94 (2018) 114–173.
[4] R. Lakes, Foam structures with a negative Poisson's ratio, Science 235 (1987) 1038–1040.
[5] K.E. Evans, M.A. Nkansah, I.J. Hutchinson, et al., Molecular network design, Nature 353 (1991) 124, 124.
[6] K.E. Evans, A. Alderson, Auxetic materials: functional materials and structures from lateral thinking!, Adv. Mater. 12 (2000) 617–628.
[7] T. Li, Y. Chen, X. Hu, et al., Exploiting negative Poisson's ratio to design 3D-printed composites with enhanced mechanical properties, Mater. Des. 142 (2018) 247–258.
[8] T. Li, F. Liu, L. Wang, Enhancing indentation and impact resistance in auxetic composite materials, Compos. Part B Eng. 198 (2020) 108229.
[9] Y. Luo, K. Yuan, L. Shen, et al., Sandwich panel with in-plane honeycombs in different Poisson's ratio under low to medium impact loads, Rev. Adv. Mater. Sci. 60 (2021) 145–157.
[10] J. Liu, W. Chen, H. Hao, et al., In-plane crushing behaviors of hexagonal honeycombs with different Poisson's ratio induced by topological diversity, Thin-Walled Struct. 159 (2021) 107223.
[11] R. Almgren, An isotropic three-dimensional structure with Poisson's ratio =?1, J. Elast. 15 (1985) 427–430. Almgren R. An isotropic three-dimensional structure with Poisson's ratio =?1.
[12] Larsen U.D., Sigmund O., Bouwstra S. Design and Fabrication of Compliant Micromechanisms and Structures with Negative Poisson's Ratio. J Microelectromechanical. Syst. 6.
[13] F. Mustahsan, S.Z. Khan, A.A. Zaidi, et al., Re-entrant honeycomb auxetic structure with enhanced directional properties, Materials 15 (2022) 8022.

[14] P.S. Theocaris, G.E. Stavroulakis, P.D. Panagiotopoulos, Negative Poisson's ratios in composites with star-shaped inclusions: a numerical homogenization approach, Arch. Appl. Mech. Ing. Arch. 67 (1997) 274–286.
[15] K.E. Evans, A. Alderson, F.R. Christian, Auxetic two-dimensional polymer networks. An example of tailoring geometry for specific mechanical properties, J. Chem. Soc. Faraday Trans. 91 (1995) 2671.
[16] D. Prall, R.S. Lakes, Properties of a chiral honeycomb with a Poisson's ratio of -1, Int J. Mech. Sci. 39 (1997) 305–314.
[17] N.J. Grima, R. Gatt, P.S. Farrugia, On the properties of auxetic meta-tetrachiral structures, Phys. Status Solidi B 245 (2008) 511–520.
[18] A. Alderson, K.L. Alderson, G. Chirima, et al., The in-plane linear elastic constants and out-of-plane bending of 3-coordinated ligament and cylinder-ligament honeycombs, Compos Sci. Technol. 70 (2010) 1034–1041.
[19] A. Alderson, K.L. Alderson, D. Attard, et al., Elastic constants of 3-, 4- and 6-connected chiral and anti-chiral honeycombs subject to uniaxial in-plane loading, Compos. Sci. Technol. 70 (2010) 1042–1048.
[20] L. Mizzi, D. Attard, R. Gatt, et al., An analytical and finite element study on the mechanical properties of irregular hexachiral honeycombs, Smart Mater. Struct. 27 (2018) 105016.
[21] L.L. Hu, Z.J. Wu, M.H. Fu, Mechanical behavior of anti-trichiral honeycombs under lateral crushing, Int. J. Mech. Sci. 140 (2018) 537–546.
[22] N. Novak, L. Biasetto, P. Rebesan, et al., Experimental and computational evaluation of tensile properties of additively manufactured hexa- and tetrachiral auxetic cellular structures, Addit. Manuf. 45 (2021) 102022.
[23] W. Wu, W. Hu, G. Qian, et al., Mechanical design and multifunctional applications of chiral mechanical metamaterials: a review, Mater. Des. 180 (2019) 107950.
[24] K.K. Dudek, R. Gatt, K.W. Wojciechowski, et al., Self-induced global rotation of chiral and other mechanical metamaterials, Int J. Solids Struct. (2020) 191–192, 212–219.
[25] D. Mousanezhad, B. Haghpanah, R. Ghosh, et al., Elastic properties of chiral, anti-chiral, and hierarchical honeycombs: a simple energy-based approach, Theor. Appl. Mech. Lett. 6 (2016) 81–96.
[26] L. Mizzi, L. Grasselli, A. Spaggiari, et al., Design of isotropic 2D chiral metamaterials based on monohedral pentagonal tessellations, Thin-Walled Struct. 187 (2023) 110739.
[27] Lim T.-C. Mechanics of Metamaterials with Negative Parameters. Singapore: Springer Singapore. Epub ahead of print 2020. DOI: 10.1007/978-981-15-6446-8.
[28] K.W. Wojciechowski, Two-dimensional isotropic system with a negative poisson ratio, Phys. Lett. A 137 (1989) 60–64.
[29] W. Zhang, Y. Wang, Z. Li, et al., Design, analysis and optimization of the uniaxial properties of a new auxetic anti-chiral parallelogram metamaterial, Thin-Walled Struct. 202 (2024) 112119.
[30] A.M. Caporale, A. Airoldi, N. Novak, A novel body centered cubic 3D auxetic chiral geometry, Smart Mater. Struct. 34 (2025) 015050.
[31] J.N. Grima, K.E. Evans, Auxetic behavior from rotating squares, J. Mater. Sci. Lett. 19 (2000) 1563–1565.
[32] L. Mizzi, A. Spaggiari, Lightweight mechanical metamaterials designed using hierarchical truss elements, Smart Mater. Struct. 29 (2020) 105036.
[33] J. N. Grima, R. Gatt, A. Alderson, et al., On the auxetic properties of `rotating rectangles' with different connectivity, J. Phys. Soc. Jpn. 74 (2005) 2866–2867.
[34] T. Lim, Auxetic system based on rotating hexagons and triangles, Phys. Status Solidi B 261 (2024) 2300586.
[35] D. Attard, J.N. Grima, A three-dimensional rotating rigid units network exhibiting negative Poisson's ratios, Phys. Status Solidi B 249 (2012) 1330–1338.
[36] Y. Gao, X. Wei, X. Han, et al., Novel 3D auxetic lattice structures developed based on the rotating rigid mechanism, Int. J. Solids Struct. 233 (2021) 111232.
[37] D. Attard, E. Manicaro, J.N. Grima, On rotating rigid parallelograms and their potential for exhibiting auxetic behaviour, Phys. Status Solidi B 246 (2009) 2033–2044.
[38] K.K. Dudek, J.A.I. Martinez, G. Ulliac, et al., Micro-scale mechanical metamaterial with a controllable transition in the poisson's ratio and band gap formation, Adv. Mater. 35 (2023) 1–10.
[39] M. Taylor, L. Francesconi, M. Gerendás, et al., Low porosity metallic periodic structures with negative Poisson's ratio, Adv. Mater. 26 (2014) 2365–2370.
[40] D. Yang, L. Jin, R.V. Martinez, et al., Phase-transforming and switchable metamaterials, Extrem. Mech. Lett. 6 (2016) 1–9.
[41] Z.-Y. Li, X.-T. Wang, L. Ma, et al., Auxetic and failure characteristics of composite stacked origami cellular materials under compression, Thin-Walled Struct. 184 (2023) 110453.
[42] H. Yasuda, J. Yang, Reentrant origami-based metamaterials with negative Poisson's ratio and bistability, Phys. Rev. Lett. 114 (2015) 185502.
[43] L.J. Gibson, M.F. Ashby, G.S. Schajer, et al., The mechanics of two dimensional cellular materials, Proc. R. Soc. A 382 (1982) 25–42.
[44] I.G. Masters, K.E. Evans, Models for the elastic deformation of honeycombs, Compos. Struct. 35 (1996) 403–422.
[45] J.N. Grima, K.E. Evans, Auxetic behavior from rotating triangles, J. Mater. Sci. 41 (2006) 3193–3196.
[46] L. Mizzi, A. Spaggiari, Chiralisation of Euclidean polygonal tessellations for the design of new auxetic metamaterials, Mech. Mater. 153 (2021) 103698.
[47] L. Mizzi, A. Spaggiari, Novel chiral honeycombs based on octahedral and dodecahedral Euclidean polygonal tessellations, Int. J. Solids Struct. 238 (2022) 111428.
[48] R. Fathauer, Tessellations: Mathematics, Art, and Recreation, CRC Press, Boca Raton, 2021.
[49] B. Grunbaum, G.C. Shephard. Tilings and Patterns, 2nd ed., Dover Books, 1987.
[50] L. Mizzi, L. Grasselli, A. Spaggiari, Clockwise vs anti-clockwise chiral metamaterials: influence of base tessellation symmetry and rotational direction of chiralisation on mechanical properties, Thin-Walled Struct. 205 (2024) 112381.
[51] Barlat F., Lian J. Mechanical APDL Element Reference.
[52] Data sheet for Onyx material, https://markforged.com/it/materials/plastics/onyx (Accessed 13 March 2025).
[53] L. Mizzi, D. Attard, R. Gatt, et al., Implementation of periodic boundary conditions for loading of mechanical metamaterials and other complex geometric microstructures using finite element analysis, Eng. Comput. 37 (2021) 1765–1779.
[54] T.C.T. Ting, T. Chen, Poisson's ratio for anisotropic elastic materials can have no bounds, Q J. Mech. Appl. Math. 58 (2005) 73–82.
[55] E. Gao, R. Li, S. Fang, et al., Bounds on the in-plane Poisson's ratios and the in-plane linear and area compressibilities for sheet crystals, J. Mech. Phys. Solids 152 (2021) 104409.
[56] G.W. Milton, Composite materials with poisson's ratios close to — 1, J. Mech. Phys. Solids 40 (1992) 1105–1137.
[57] J.H. Conway, H. Burgiel, C. Goodman-Strauss, The Symmetries of Things, CRC Press, 2008.